Materials Science and Engineering A 549 (2012) 43–49

Contents lists available at SciVerse ScienceDirect

Materials Science and Engineering A

journal homepage: www.elsevier.com/locate/msea

Microstructure and mechanical properties of three porous Si_3N_4 ceramics fabricated by different techniques

Xiangming Li [a,*], Litong Zhang [b], Xiaowei Yin [b]

[a] College of Water Resources and Architecture Engineering, Northwest Agriculture and Forestry University, Yangling, Shaanxi 712100, PR China
[b] National Key Laboratory of Thermostructure Composite Materials, Northwestern Polytechnical University, Xi'an, Shaanxi 710072, PR China

ARTICLE INFO

Article history:
Received 5 February 2012
Received in revised form 4 March 2012
Accepted 22 March 2012
Available online 16 April 2012

Keywords:
Si_3N_4
Porous
Microstructure
Mechanical property

ABSTRACT

Three porous Si_3N_4 ceramics were fabricated using the same starting Si_3N_4 powder by techniques of (1) oxidation-bonding combined with sol–gel infiltration sintering (OB-IS), (2) cold-pressing combined with pressureless-sintering (CP-PS), and (3) 3D-printing combined with pressureless-sintering (3DP-PS). Due to the obvious difference in microstructure, phase composition, linear shrinkage, pore size distribution and porosity, the three porous Si_3N_4 ceramics possess characteristic in mechanical properties. Si_3N_4-(OB-IS) possesses lower flexural strength (23–120 MPa), fracture toughness (0.4–1.4 MPa $m^{1/2}$) and Young's modulus (9.1–26.3 GPa) but the highest Vickers hardness (1.1–4.1 GPa). Si_3N_4-(CP-PS) possesses the highest flexural strength (143–207 MPa), fracture toughness (2.3–3.4 MPa $m^{1/2}$) and Young's modulus (45.8–58.5 GPa) but lower Vickers hardness (0.8–1.1 GPa). Si_3N_4-(3DP-PS) possesses the lowest flexural strength (13 MPa), fracture toughness (0.3 MPa $m^{1/2}$), Young's modulus (3.9 GPa) and Vickers hardness (0.4 GPa).

1. Introduction

Silicon nitride (Si_3N_4) ceramics are one of the most promising thermal structural materials for various applications at elevated temperatures due to excellent mechanical properties, low coefficient of thermal expansion (CTE) and good resistance to thermal shock [1–6]. Recently, in order to meet some special applications, Si_3N_4 ceramics with high porosity have attracted many attentions [7–11]. For engineering applications, such as separation membranes, catalyst supports and gas filters, porous Si_3N_4 ceramics with high porosity of channels and a well-controlled pore size distribution are required. In other words, porous Si_3N_4 ceramics with a tailored microstructure are necessary [12].

So far, various techniques have been developed to fabricate porous Si_3N_4 ceramics [12–16]. Though using the same starting Si_3N_4 powder, the porous Si_3N_4 ceramics fabricated by different techniques show different mechanical properties due to the difference of microstructure, pore size distribution and porosity [17]. In the present paper, three porous Si_3N_4 ceramics are fabricated using the same starting Si_3N_4 powder by different techniques: (1) oxidation-bonding combined with sol–gel infiltration sintering, (2) cold-pressing combined with pressureless-sintering, and (3) 3D-printing combined with pressureless-sintering. The microstructure, phase composition, linear shrinkage, pore size distribution, porosity and mechanical properties of the three porous Si_3N_4 ceramics are measured. The reasons causing the difference in mechanical properties of the three porous Si_3N_4 ceramics are analyzed in detail.

2. Experimental procedure

2.1. Fabrication techniques

2.1.1. Oxidation-bonding combined with sol–gel infiltration sintering

Si_3N_4 powder (α-Si_3N_4(>90 wt.%), Si(<0.1 wt.%)) with a mean particle size of 0.3 μm, supplied by Kingsway Ceramic Co. Ltd., Shanghai, China, was mixed with 15 wt% phenolic resin in ethanol into slurry. The slurry was ball-milled for 24 h and dried at 90 °C for 10 h. The powder blend was crushed, passed through a 50 mesh sieve, and then cold-pressed into preforms under a pressure of 100 MPa using a rectangular steel die. Oxidation-bonding porous Si_3N_4 ceramic (Si_3N_4-(OB)) was fabricated by oxidizing the preform at 1250 °C for 2 h in air. The Si_3N_4-(OB) specimens were hung in a closed glass container half full with silica sol. Vacuumized the container to pressure lower than 5 kPa, then submerged the specimens in silica sol and hold for 15 min. Restore the pressure of the container to normal. After 15 min of that, the specimens were taken out and ultrasonically washed in water for 5 min. The silica sol in Si_3N_4-(OB) turned into silica gel by holding the temperature at 90 °C

* Corresponding author. Tel.: +86 029 87082902; fax: +86 029 87082901.
E-mail address: li_xiangming@yahoo.com (X. Li).

0921-5093/$ – see front matter © 2012 Elsevier B.V. All rights reserved.
http://dx.doi.org/10.1016/j.msea.2012.03.114

for 10 h. The amount of silica gel in Si_3N_4-(OB) was increased by repeating above infiltration procedure. Finally, the Si_3N_4-(OB) infiltrated with different amount of silica gel was sintered at 1250 °C for 2 h in N_2. The Si_3N_4-(OB) after sintering process is named as Si_3N_4-(OB-IS).

2.1.2. Cold-pressing combined with pressureless-sintering

Si_3N_4 powder was mixed with 5 wt% Lu_2O_3 and phenolic resin ranging from 5 to 35 wt% in ethanol, ball milled the slurry for 24 h and dried at 90 °C for 10 h. The powder blend was crushed, passed through a 50 mesh sieve, and then cold-pressed into preforms under a pressure of 100 MPa using a rectangular steel die. The preforms were pre-oxidized at 800 °C for 5 h in air, and then pressureless-sintered in a furnace at 1800 °C for 2 h under a nitrogen atmosphere pressure of 0.3 MPa. The porous Si_3N_4 ceramic fabricated by above process is named as Si_3N_4-(CP-PS).

2.1.3. 3D-printing combined with pressureless-sintering

Si_3N_4 powder was mixed with 5 wt% Lu_2O_3 and 10 wt% dextrin in distilled water, ball milled the slurry for 24 h and dried at 90 °C for 10 h. The powder blend was crushed, passed through a 60 mesh sieve, and then fabricated into preforms by 3D-printing which were carried out on a 3D-printer (Spectrum Z510, Z Corporation, USA) using the water based printer solution (ZB60, Z Corporation, USA). During printing, the layer thickness and shell/core binder saturation were set to 0.1 mm and 2/2, respectively. The printed preforms were dried in the powder bed at 60 °C for 20 h. After 3D-printing, the preforms were oxidized at 800 °C for 5 h in air, and then pressureless-sintered in a furnace at 1800 °C for 2 h under a nitrogen atmosphere pressure of 0.3 MPa. The porous Si_3N_4 ceramic fabricated by above process is named as Si_3N_4-(3DP-PS).

2.2. Characterization

The porosity and density were measured by Archimedes method. The pore size distribution was measured by mercury porosimeter (Poremaster 33, Quantachrome Instruments Co., Boynton Beach, FL, USA). Phase analyse was conducted by X-ray diffraction (XRD), via a computer-controlled diffractometer (X'Pert Pro, Philips, Netherlands). Microstructure was observed by scanning electron microscopy (S-4700, Hitachi, Japan).

Using SANS CMT4304 instrument (Sans Materials Testing Co., Shenzhen, China), the flexural strength (σ) of the specimens with dimension of 3 mm × 4 mm × 40 mm was evaluated via the three-point bending test with a support distance of 30 mm and a loading speed of 0.5 mm/min, Young's modulus (E) was calculated according to the stress–strain curve during flexural strength test. The fracture toughness (K_{IC}) of the specimens with dimension of 2.5 mm × 5 mm × 30 mm and notch length of 2.5 mm was tested by single edge notched beam (SENB) method. The average values of flexural strength and fracture toughness were obtained by testing five specimens. Vickers hardness (HV) was measured using a digital hardness tester with a pyramidal Vickers indenter. The specimens were indented with loads of 5 kg for 15 s and an average of eight indents was analyzed.

3. Results and discussion

3.1. Microstructure

The bulk density of the preform fabricated by cold-pressing is high, and the particles stack compactly with each other. In order to fabricate porous Si_3N_4 ceramic, there should be adequate space among α-Si_3N_4 particles, so the role of phenolic resin in raw material for Si_3N_4-(OB-IS) and Si_3N_4-(CP-PS) is pore-forming agent. The bulk density of the preform fabricated by 3D-printing is low, and the particles stack incompactly with each other. In order to make the preform not broken when it being taken out from powder bed, there should be adequate bonding strength among α-Si_3N_4 particles, so the role of dextrin in raw material for Si_3N_4-(3DP-PS) is bonding agent.

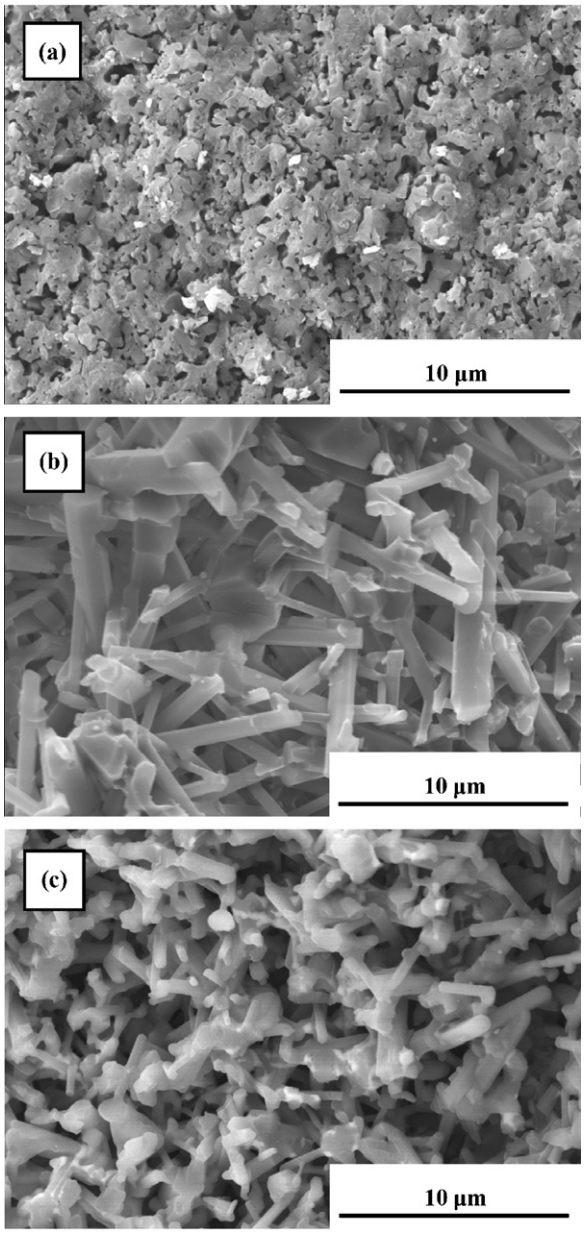

Fig. 1. Micrographs of (a) Si_3N_4-(OB-IS), (b) Si_3N_4-(CP-PS) and (c) Si_3N_4-(3DP-PS).

Fig. 1 shows the micrographs of Si_3N_4-(OB-IS), Si_3N_4-(CP-PS) and Si_3N_4-(3DP-PS). As can be seen, the microstructures of the three porous Si_3N_4 ceramics are much different with each other. The pores in Si_3N_4-(OB-IS) are formed by stacking α-Si_3N_4 particles bonded by SiO_2. The SiO_2 derives from the oxidation of Si_3N_4 and the sintering of silica gel. The pores in Si_3N_4-(CP-PS) are formed by intercrossing rod-like β-Si_3N_4 particles with each other. The rod-like β-Si_3N_4 particles derive from the transformation of α-Si_3N_4 particles during sintering process. Si_3N_4-(3DP-PS) and Si_3N_4-(CP-PS) are fabricated by the same sintering process. The α-Si_3N_4 particles in the preform of Si_3N_4-(CP-PS) are cold-pressed compactly with each other, while the α-Si_3N_4 particles in the preform of Si_3N_4-(3DP-PS)

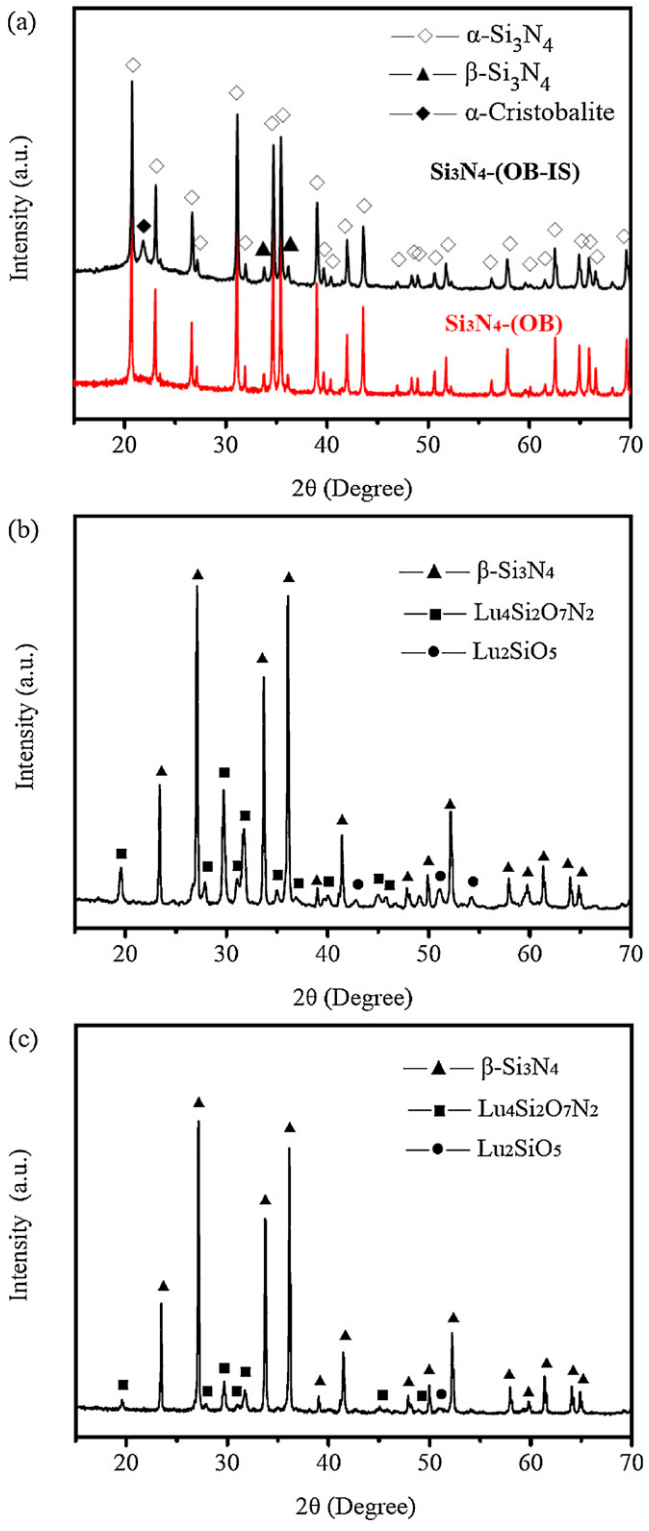

Fig. 2. XRD patterns of (a) Si_3N_4-(OB-IS), (b) Si_3N_4-(CP-PS) and (c) Si_3N_4-(3DP-PS).

stack incompactly with each other, so the pores in Si_3N_4-(3DP-PS) are bigger than that in Si_3N_4-(CP-PS).

3.2. Phase composition

Fig. 2 shows the XRD pattern of Si_3N_4-(OB-IS), Si_3N_4-(CP-PS) and Si_3N_4-(3DP-PS). As shown in Fig. 2(a), Si_3N_4-(OB) is mainly composed of α-Si_3N_4 and β-Si_3N_4. Phenolic resin-derived pyrolysis carbon (PyC) can restrain the devitrification of SiO_2 [18], so no cristobalite peak appears in the XRD pattern of Si_3N_4-(OB). Nitrogen shows poor restraining effect on the devitrification of SiO_2 [18], so there is a low cristobalite peak appears in the XRD pattern of Si_3N_4-(OB-IS). As shown in Fig. 2(a), Si_3N_4-(OB-IS) is composed of α-Si_3N_4, β-Si_3N_4, cristobalite and a small amount of amorphous SiO_2.

Si_3N_4-(CP-PS) and Si_3N_4-(3DP-PS) are fabricated by different preforming technique but by the same sintering process, so the phase composition of Si_3N_4-(CP-PS) and Si_3N_4-(3DP-PS) is the same with each other. As shown in Fig. 2(b) and (c), the primary phase of Si_3N_4-(CP-PS) and Si_3N_4-(3DP-PS) is β-Si_3N_4, the secondary phase is $Lu_4Si_2O_7N_2$ with a small amount of Lu_2SiO_5. Only β-Si_3N_4 phase is detected though the starting powder is α-Si_3N_4, which indicates that a complete α → β transformation occurred during sintering process. The phase transformation of Si_3N_4 from α → β takes place by (a) dissolution of α phase and saturation of viscous liquid phase, (b) transport of Si and N ions through the viscous liquid phase, and (c) attachment onto existing β particles or grains [19]. During sintering process, $Lu_4Si_2O_7N_2$ is formed by reaction of Lu_2O_3 and SiO_2 on the surface of Si_3N_4 particles [20]. At the same time of promoting the sintering of Si_3N_4 particles, $Lu_4Si_2O_7N_2$ is helpful for phase transformation of Si_3N_4 from α → β [21,22]. Because of the different stack density of Si_3N_4 powders in the preform, the content of $Lu_4Si_2O_7N_2$ in Si_3N_4-(3DP-PS) is lower than that in Si_3N_4-(CP-PS).

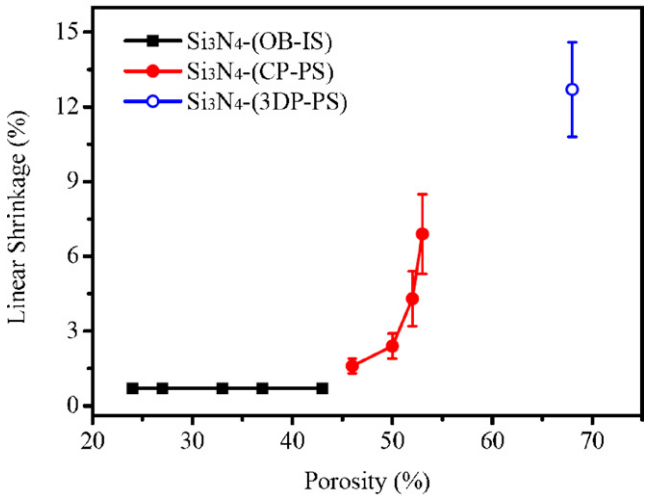

Fig. 3. Linear shrinkage of Si_3N_4-(OB-IS), Si_3N_4-(CP-PS) and Si_3N_4-(3DP-PS).

3.3. Linear shrinkage

Fig. 3 shows the linear shrinkage of Si_3N_4-(OB-IS), Si_3N_4-(CP-PS) and Si_3N_4-(3DP-PS). At the beginning of oxidation-bonding process, the α-Si_3N_4 particles in the preform of Si_3N_4-(OB) is fixed quickly by the oxidation-derived SiO_2, so the linear shrinkage of as-obtained Si_3N_4-(OB) is only 0.7%. Once the α-Si_3N_4 particles in Si_3N_4-(OB) have been fixed by SiO_2, the dimension of Si_3N_4-(OB-IS) will remain unchanged after sintering process.

$Lu_4Si_2O_7N_2$ is a viscous liquid phase at high temperature [20] and the melting temperature of the $Lu_4Si_2O_7N_2$ phase is higher than 1850 °C [23]. The existence of $Lu_4Si_2O_7N_2$ is the key reason causing the linear shrinkage of Si_3N_4-(CP-PS). Due to the dissolution of Si_3N_4 in viscous liquid phase, the β-Si_3N_4 particles are dragged close with each other by viscous liquid phase during sintering process. During oxidation process, the phenolic resin in the preform of Si_3N_4-(CP-PS) is oxidized and removed in the form of CO or CO_2. The more phenolic resin is added in the preform, the more linear shrinkage the Si_3N_4-(CP-PS) shows. As the content of

Table 1
Porosity of Si_3N_4-(OB-IS), Si_3N_4-(CP-PS) and Si_3N_4-(3DP-PS).

Si_3N_4-(OB-IS)					
Cycles of sol–gel infiltration	0	1	2	3	4
Porosity (%)	43	37	33	28	24
Si_3N_4-(CP-PS)					
Content of phenolic resin (wt%)	5	15	25	35	
Porosity (%)	46	50	52	53	
Si_3N_4-(3DP-PS)					
Porosity (%)	68				

phenolic resin in preform increases from 5 to 35 wt%, the linear shrinkage of Si_3N_4-(CP-PS) increases obviously from 1.6 to 6.9%. Because of the same composition and sintering process, the reason causing the linear shrinkage of Si_3N_4-(3DP-PS) is the same with that of Si_3N_4-(CP-PS). The α-Si_3N_4 particles in the preform of Si_3N_4-(3DP-PS) stack incompactly with each other, so there is more space for β-Si_3N_4 particles in Si_3N_4-(3DP-PS) to move close. The linear shrinkage of Si_3N_4-(3DP-PS) is 12.7%, which is much larger than that of Si_3N_4-(CP-PS).

3.4. Pore size distribution and porosity

Fig. 4 shows the pore size distribution of Si_3N_4-(OB-IS), Si_3N_4-(CP-PS) and Si_3N_4-(3DP-PS). Due to the different fabrication technique, the three porous Si_3N_4 ceramics show different pore size distribution. The mean pore size in as-obtained Si_3N_4-(OB) is 0.6 μm. The mean pore size in Si_3N_4-(OB-IS) decreases from 0.4 to 0.2 μm with the increase of sol–gel infiltration cycles from one to four. With the increase of phenolic resin content from 5 to 35 wt%, the mean pore size in Si_3N_4-(CP-PS) increases from 1 to 2 μm. The mean pore size in Si_3N_4-(3DP-PS) is 4 μm. The result shown in Fig. 4 is identical with that shown Fig. 1.

Table 1 lists the porosity of Si_3N_4-(OB-IS), Si_3N_4-(CP-PS) and Si_3N_4-(3DP-PS). The porosity of as-obtained Si_3N_4-(OB) is 43%. As the sol–gel infiltration cycle increases from one to four, the porosity of Si_3N_4-(OB-IS) decreases from 37 to 24%. As the content of phenolic resin increases from 5 to 35 wt%, the porosity of Si_3N_4-(CP-PS) increases from 46 to 53%. The α-Si_3N_4 particles in the preform of Si_3N_4-(3DP-PS) stack incompactly with each other, so the porosity of Si_3N_4-(3DP-PS) is high as 68%.

3.5. Mechanical properties

Figs. 5 and 6 show the flexural strength and fracture toughness of Si_3N_4-(OB-IS), Si_3N_4-(CP-PS) and Si_3N_4-(3DP-PS) as functions of porosity. The flexural strength and fracture toughness of the three porous Si_3N_4 ceramics decrease in similar trend with the increase of porosity, but the reasons resulting in above trends are different. As to Si_3N_4-(OB) and Si_3N_4-(OB-IS), the decreases of flexural strength and fracture toughness are codetermined by the change of porosity, pore size and SiO_2 content. The pores in as-obtained Si_3N_4-(OB) are big and irregular, and there are many sharp angles around the pores, resulting in easy propagation of crack in Si_3N_4-(OB) during test. The flexural strength and fracture toughness of Si_3N_4-(OB) are low as 23 MPa and 0.4 MPa $m^{1/2}$ respectively. By increasing sol–gel infiltration cycle, the SiO_2 content in Si_3N_4-(OB-IS) increases, making it difficult for crack to propagate in Si_3N_4-(OB-IS) during test. With the decrease of porosity from 37 to 24%, Si_3N_4-(OB-IS) improves obviously in flexural strength from 40 to 120 MPa and in fracture toughness from 0.5 to 1.4 MPa $m^{1/2}$.

The decrease of Si_3N_4-(CP-PS) in flexural strength and fracture toughness is due to the increase of porosity. With the increase

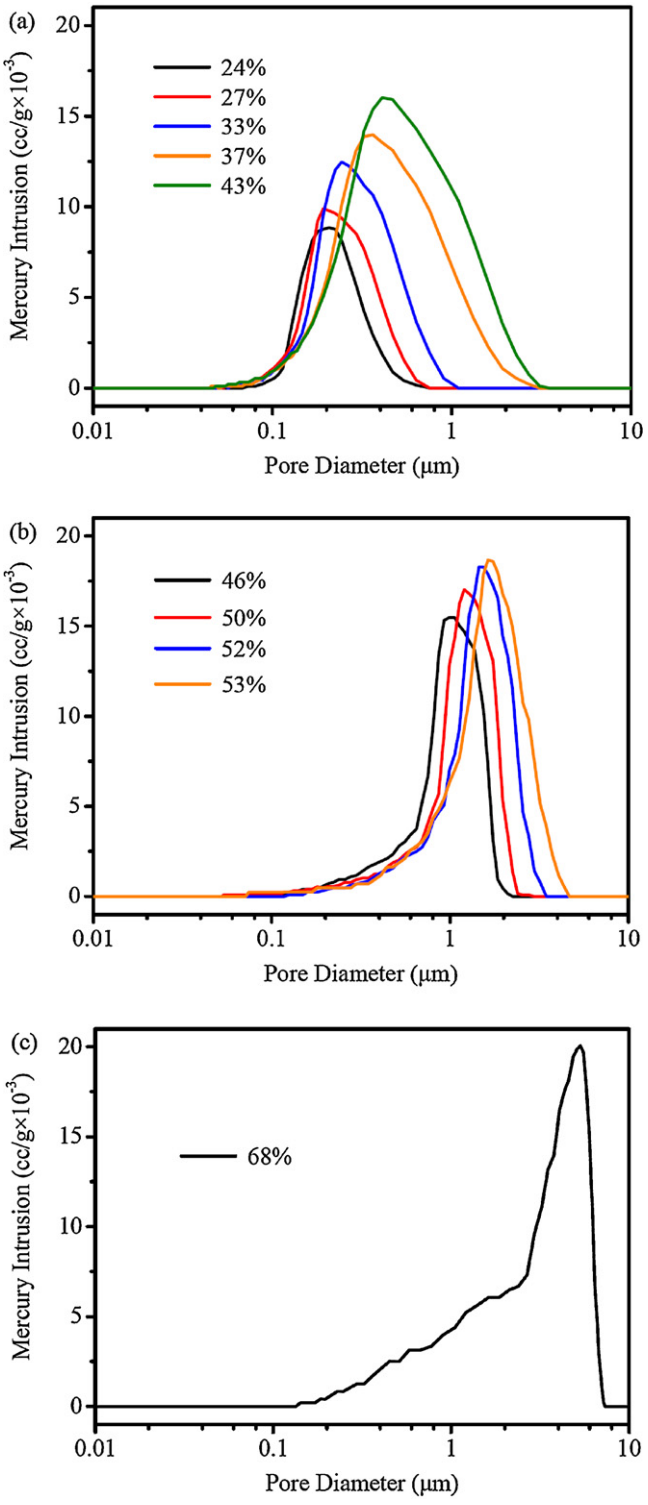

Fig. 4. Pore size distribution of (a) Si_3N_4-(OB-IS), (b) Si_3N_4-(CP-PS) and (c) Si_3N_4-(3DP-PS).

of porosity from 46 to 53%, Si_3N_4-(CP-PS) decreases in flexural strength from 207 to 143 MPa and in fracture toughness from 3.4 to 2.3 MPa $m^{1/2}$. Si_3N_4-(CP-PS) possesses bigger pores and higher porosity than Si_3N_4-(OB-IS), but Si_3N_4-(CP-PS) possesses higher flexural strength and fracture toughness than Si_3N_4-(OB-IS) due to the good load-bearing ability of rod-like β-Si_3N_4 particles.

Because of the insufficiency of $Lu_4Si_2O_7N_2$ in Si_3N_4-(3DP-PS), the β-Si_3N_4 particles in Si_3N_4-(3DP-PS) are malformed and

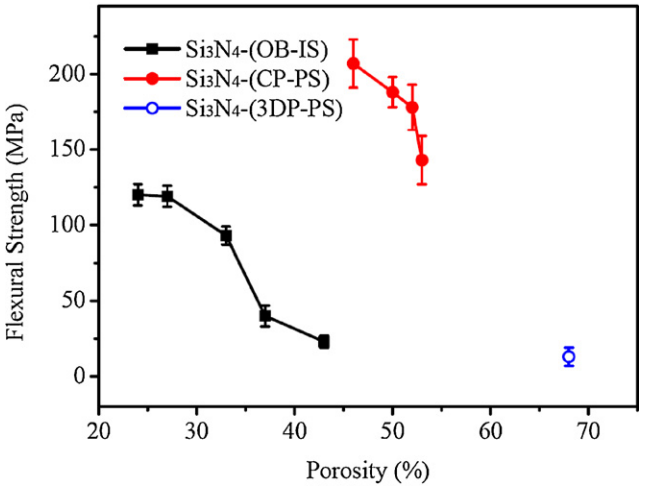

Fig. 5. Flexural strength of Si_3N_4-(OB-IS), Si_3N_4-(CP-PS) and Si_3N_4-(3DP-PS) as functions of porosity.

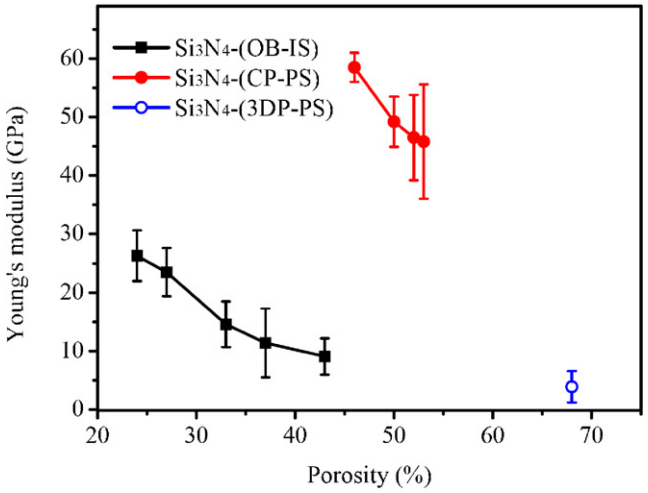

Fig. 7. Young's modulus of Si_3N_4-(OB-IS), Si_3N_4-(CP-PS) and Si_3N_4-(3DP-PS) as functions of porosity.

immature-grown. As can be seen by comparing Fig. 1(b) and (c), the β-Si_3N_4 particles in Si_3N_4-(3DP-PS) are much shorter than those in Si_3N_4-(CP-PS), so the load-bearing ability of β-Si_3N_4 particles in Si_3N_4-(3DP-PS) are much lower than that of β-Si_3N_4 particles in Si_3N_4-(CP-PS). The flexural strength and fracture toughness of Si_3N_4-(3DP-PS) are only 13 MPa and 0.3 MPa $m^{1/2}$, respectively.

Fig. 7 shows the Young's modulus of Si_3N_4-(OB-IS), Si_3N_4-(CP-PS) and Si_3N_4-(3DP-PS) as functions of porosity. The Young's modulus which is calculated according to the stress–strain curve during flexural strength test is great affected by flexural strength, so the Young's modulus and flexural strength of the three porous Si_3N_4 ceramics decrease also in similar trend with the increase of porosity. Due to the high porosity and immature-grown β-Si_3N_4 particles, Si_3N_4-(3DP-PS) possesses a very low Young's modulus as 3.9 GPa. The main composition is β-Si_3N_4 in Si_3N_4-(CP-PS), and there is no composition change as the porosity decreases from 53 to 46%, so the Young's modulus of Si_3N_4-(CP-PS) increases rapidly from 45.8 to 58.5 GPa with the decrease of porosity from 53 to 46%. The Young's modulus of SiO_2 is much lower than that of Si_3N_4. Calculating according to the weight change after fabrication process, there is about 26 vol.% SiO_2 in as-obtained Si_3N_4-(OB), so the Young's modulus of Si_3N_4-(OB) with porosity of 43% is only 9.1 GPa which is much lower than that of Si_3N_4-(CP-PS) with porosity of 46%. In addition, the decrease of porosity in Si_3N_4-(OB-IS) is due to the increase of SiO_2 content, so the Young's modulus of Si_3N_4-(OB-IS) increases slowly from 11.4 to 26.3 GPa with the rapid decrease of porosity from 43 to 24%.

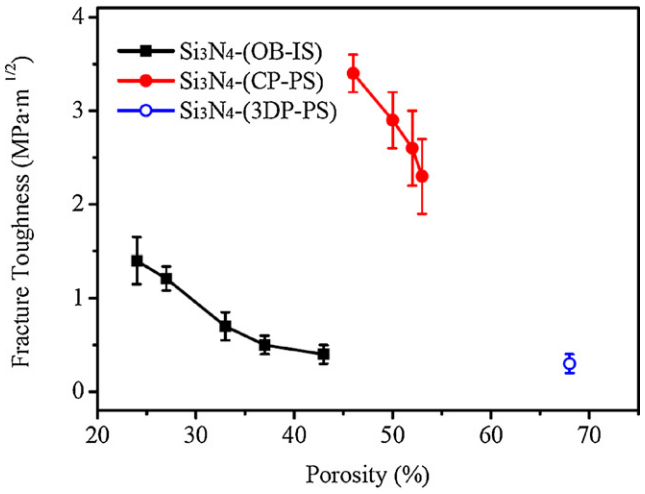

Fig. 6. Fracture toughness of Si_3N_4-(OB-IS), Si_3N_4-(CP-PS) and Si_3N_4-(3DP-PS) as functions of porosity.

Fig. 8 shows the micrographs of the indent at the surface of Si_3N_4-(OB-IS), Si_3N_4-(CP-PS) and Si_3N_4-(3DP-PS). After indentation with the same loads, the indent at the surface of Si_3N_4-(CP-PS) is smaller than that at the surface of Si_3N_4-(3DP-PS) while bigger than that at the surface of Si_3N_4-(OB-IS). Calculating according to the diagonal length of the indent, the Vickers hardness of Si_3N_4-(OB-IS), Si_3N_4-(CP-PS) and Si_3N_4-(3DP-PS) as functions of porosity is shown in Fig. 9. As to Si_3N_4-(OB-IS), the resistance to the pressure force originating from indenter increases with the increase of SiO_2 content, so the Si_3N_4-(OB-IS) increases rapidly in Vickers hardness from 1.1 to 4.1 GPa with the decrease of porosity from 43 to 24%. The increase of Si_3N_4-(CP-PS) and Si_3N_4-(3DP-PS) in Vickers hardness is due to the increase of the number of β-Si_3N_4 particles per unit bulk as the porosity decreases. Due to the little decrease of porosity from 53 to 46%, the Si_3N_4-(CP-PS) increases slightly in Vickers hardness from 0.8 to 1.1 GPa. Because of the higher porosity, Si_3N_4-(3DP-PS) possesses a lower Vickers hardness of 0.4 GPa. Basically, without consideration of preforming technique, the Vickers hardness of the three porous Si_3N_4 ceramics increases with the decrease of porosity.

The Vickers indentation fracture toughness (VIF) test has been a popular experimental technique for the estimate of the fracture resistance of brittle ceramics for the past three decades [24–32,15]. In VIF technique, the fracture toughness is calculated by measuring the length of the cracks formed during Vickers hardness test using Niihara's equation as follows: [33–35]

$$K_{IC} = \xi\left(\frac{E}{H}\right)^{2/5}\frac{P}{al^{1/2}} \quad (0.25 < l/a < 2.5) \tag{1}$$

$$K_{IC} = \xi\left(\frac{E}{H}\right)^{1/2}\frac{P}{(1+a)^{3/2}} \quad (l/a > 2.5), \tag{2}$$

where l is the crack length, a is the half diagonal of the indent, E is the Young's modulus, H is the Vickers hardness, P is the applied load and ξ is a constant that depends on the indenter geometry and assumptions. l and a are exactly measured by using scanning electron microscopy (SEM).

Because the complex crack network and residual stress damage zone around indentations are not amenable to a straightforward analysis as in most traditional fracture mechanics test

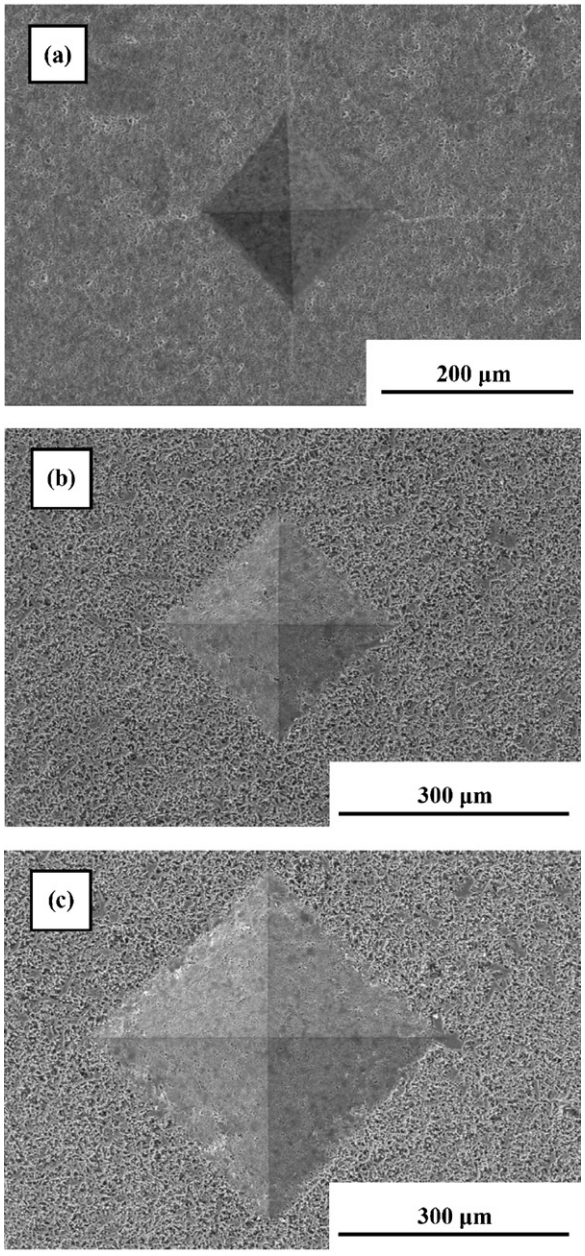

Fig. 8. Micrographs of the indent at the surface of (a) Si_3N_4-(OB-IS), (b) Si_3N_4-(CP-PS) and (c) Si_3N_4-(3DP-PS).

configurations [36,37], the fracture toughness value measured by VIF is far higher than that measured by SENB [38]. It has been recommended that the VIF technique no longer be acceptable for the fracture toughness testing of any dense or porous ceramic materials [36–38]. Roughly, need not know the Young's modulus, VIF technique may be used for reflecting the relation between fracture toughness and Vickers hardness of ceramic [33].

As to the ceramic dense or with low porosity, the higher the crack length is, the higher the Vickers hardness and the lower the fracture toughness will be [33]. Fig. 10 shows the micrograph of the crack propagating from one corner of the indent at the surface of Si_3N_4-(OB-IS). As can be seen, the crack is long and straight, meaning a high Vickers hardness and a low fracture toughness of the ceramic. As to the ceramic with high porosity, if indentations produce no cracks, the ceramic possesses high fracture toughness and low Vickers hardness [33]. As shown in Fig. 8(b), no crack is

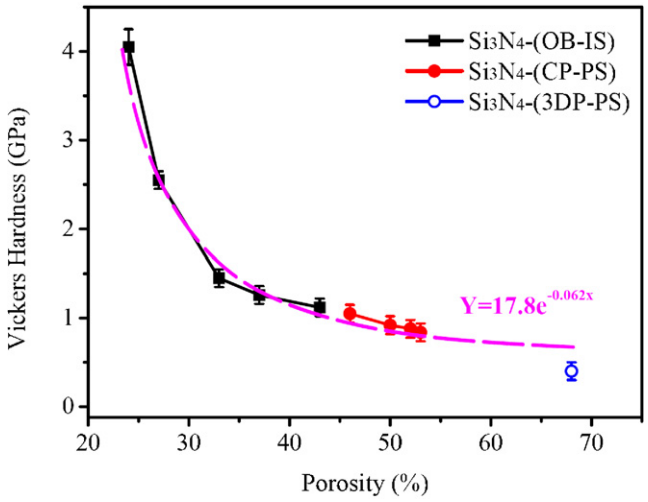

Fig. 9. Vickers hardness of Si_3N_4-(OB-IS), Si_3N_4-(CP-PS) and Si_3N_4-(3DP-PS) as functions of porosity.

detected at the corner of the indent at the surface of Si_3N_4-(CP-PS), meaning a low Vickers hardness and a high fracture toughness of the ceramic. Above is the reason why Si_3N_4-(OB-IS) possesses higher Vickers hardness but lower flexural strength and fracture toughness than Si_3N_4-(CP-PS).

The dependences of σ, K_{IC}, E and H on porosity and pore characteristic have been extensively investigated in recent years [33,39,40], and a simple expression has been proposed by Rice as follows [41]:

$$Y = Y_0 \cdot \exp(-bV_p) \quad (3)$$

where Y is σ, K_{IC}, E or H of the porous structure at a porosity V_p, b is a constant depending on the pore characteristics. The pre-exponential term Y_0 corresponds to σ, K_{IC}, E or H for compacts with no porosity.

Based on above analysis, porosity is not the only reason causing the differences in flexural strength, Young's modulus and fracture toughness of the three porous Si_3N_4 ceramics, so the σ, E and K_{IC} of the three porous Si_3N_4 ceramics do not fit Eq. (3). While the key reason causing the difference in Vickers hardness of the three porous Si_3N_4 ceramics is porosity, so the H of the three porous Si_3N_4 ceramics can be fitted according to Eq. (3). As shown in Fig. 9, the Vickers hardness of the three porous Si_3N_4 ceramics fits Eq. (3) well as the porosity increases from 24 to 68%, and the corresponding Vickers hardness of the nonporous Si_3N_4 ceramic is 17.8 GPa, which

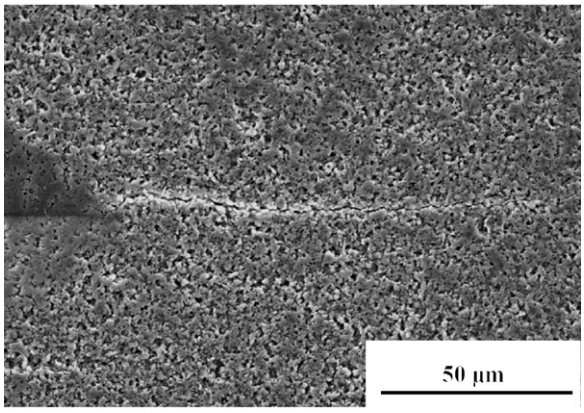

Fig. 10. Micrograph of the crack propagating from one corner of the indent at the surface of Si_3N_4-(OB-IS).

is close to the value of Vickers hardness of dense Si_3N_4 ceramic reported by other researchers [42,43].

4. Conclusions

Three porous Si_3N_4 ceramics were fabricated respectively by techniques of oxidation-bonding combined with sol–gel infiltration sintering, cold-pressing combined with pressureless-sintering, and 3D-printing combined with pressureless-sintering. Due to the difference in microstructure, phase composition, linear shrinkage, pore size distribution and porosity, the three porous Si_3N_4 ceramics show different mechanical properties.

1. As the porosity of Si_3N_4-(OB-IS) decreases from 43 to 24%, the flexural strength, fracture toughness, Young's modulus and Vickers hardness of Si_3N_4-(OB-IS) increase respectively from 23 to 120 MPa, from 0.4 to 1.4 MPa $m^{1/2}$, from 9.1 to 26.3 GPa and from 1.1 to 4.1 GPa. The key reason causing the increase of flexural strength and fracture toughness is the increase of crack propagation resistance with the increase of sol–gel infiltration cycle. Because of the low Young's modulus of SiO_2, Si_3N_4-(OB-IS) increases slowly in Young's modulus with the rapid increase of SiO_2 content. The rapid increase of Vickers hardness is due to the obvious increase of resistance to the pressure force with the increase of SiO_2 content.
2. As the porosity of Si_3N_4-(CP-PS) decreases from 46 to 53%, the flexural strength, fracture toughness, Young's modulus and Vickers hardness of Si_3N_4-(CP-PS) decrease respectively from 207 to 143 MPa, from 3.4 to 2.3 MPa $m^{1/2}$, from 45.8 to 58.5 GPa and from 1.1 to 0.8 GPa. The increase of porosity is the key reason causing the decrease in flexural strength, fracture toughness and Young's modulus. The decrease of Vickers hardness is due to the decrease of the number of β-Si_3N_4 particles per unit bulk as the porosity increases.
3. Si_3N_4-(3DP-PS) possesses high porosity as 68% because of the incompact stack of α-Si_3N_4 particles in the preform fabricated by 3D-printing. Because of the high porosity and immature-grown β-Si_3N_4 particles, Si_3N_4-(3DP-PS) shows low flexural strength, fracture toughness, Young's modulus and Vickers hardness as 13 MPa, 0.3 MPa $m^{1/2}$, 3.9 GPa and 0.4 GPa respectively.

References

[1] T. Nishimura, M. Mitomo, H. Suematsu, J. Mater. Res. 12 (1997) 203–209.
[2] H. Park, H.E. Kim, K. Niihara, J. Am. Ceram. Soc. 80 (1997) 750–756.
[3] H.J. Choi, J.G. Lee, Y.W. Kim, J. Mater. Sci. 32 (1997) 1937–1942.
[4] H. Park, H.W. Kim, H.E. Kim, J. Am. Ceram. Soc. 81 (1998) 2130–2134.
[5] H.J. Kleebe, G. Pezzotti, G. Ziegler, J. Am. Ceram. Soc. 82 (1999) 1857–1867.
[6] K.J. Yoon, S.M. Wiederthon, W.E. Luecke, J. Am. Ceram. Soc. 83 (2000) 2017–2022.
[7] Y. Shigegaki, M.E. Brito, K. Hirao, M. Toriyama, S. Kanzaki, J. Am. Ceram. Soc. 80 (1997) 495–498.
[8] C. Kawai, A. Yamakawa, J. Am. Ceram. Soc. 80 (1997) 2705–2708.
[9] Y. Inagaki, T. Ohji, S. Kanzaki, Y. Shigegaki, J. Am. Ceram. Soc. 83 (2000) 1807–1809.
[10] J.F. Yang, G.J. Zhang, T. Ohji, J. Am. Ceram. Soc. 84 (2001) 1639–1641.
[11] J.F. Yang, G.J. Zhang, T. Ohji, J. Mater. Res. 16 (2001) 1916–1918.
[12] J.F. Yang, Z.Y. Deng, T. Ohji, J. Eur. Ceram. Soc. 23 (2003) 371–378.
[13] S.Q. Ding, Y.P. Zeng, D.L. Jiang, Mater. Lett. 61 (2007) 2277–2280.
[14] J.Q. Li, F. Luo, D.M. Zhu, W.C. Zhou, Trans. Nonferrous Met. Soc. 16 (2006) 487–489.
[15] Y. Inagaki, Y. Shigegaki, M. Ando, T. Ohji, J. Eur. Ceram. Soc. 24 (2004) 197–200.
[16] A. Diaz, S. Hampshire, J. Eur. Ceram. Soc. 24 (2004) 413–419.
[17] A. Diaz, S. Hampshire, J.F. Yang, T. Ohji, S. Kanzaki, J. Am. Ceram. Soc. 88 (2005) 698–706.
[18] X.M. Li, X.W. Yin, L.T. Zhang, S.S. He, J. Non-Cryst. Solids 354 (2008) 3254–3259.
[19] W. Dressler, H.J. Kleebe, M.J. Hoffmann, M. Ruhle, G. Petzow, J. Eur. Ceram. Soc. 16 (1996) 3–14.
[20] L.U.J. Ogbuji, S.R. Bryan, J. Am. Ceram. Soc. 78 (1995) 1272–1278.
[21] D.Y. Chen, B.L. Zhang, H.R. Zhang, W.L. Li, Ceram. Int. 29 (2003) 363–364.
[22] W.K. Li, D.Y. Chen, B.L. Zhang, H.R. Zhang, W.L. Li, Mater. Lett. 58 (2004) 2322–2325.
[23] N. Hirosaki, Y. Yamamoto, T. Nishimura, M. Mitomo, J. Am. Ceram. Soc. 85 (2002) 2861–2863.
[24] S. Palmqvist, Jernkortorets Ann. 141 (1957) 300–307.
[25] A.G. Evans, E.A. Charles, J. Am. Ceram. Soc. 59 (1976) 371–372.
[26] T. Fujii, T. Nose, IJIS Int. 29 (1989) 717–725.
[27] M. Sakai, R.C. Bradt, Int. Mater. Rev. 38 (1993) 53–78.
[28] I. Yoshiyaki, N. Kindo, T. Ohji, O. Tatsuki, J. Eur. Ceram. Soc. 22 (2002) 2489–2494.
[29] J.H. She, T. Ohji, J. Mater. Sci. Lett. 21 (2002) 1833–1834.
[30] Z.Y. Deng, J. She, Y. Inagaki, J.F. Yang, T. Ohji, T. Tanaka, J. Eur. Ceram. Soc. 24 (2004) 2055–2059.
[31] Z.Y. Deng, T. Fukasawa, M. Ando, G.J. Zhang, T. Ohji, J. Am. Ceram. Soc. 84 (2001) 2638–2644.
[32] J.H. She, T. Ohji, Mater. Chem. Phys. 80 (2003) 610–614.
[33] R. Kumar, K.H. Prakash, P. Cheang, K.A. Khor, Acta Mater. 53 (2005) 2327–2335.
[34] K. Niihara, J. Mater. Sci. Lett. 2 (1983) 221–223.
[35] K. Niihara, R. Morena, D.P.H. Hasselman, J. Mater. Sci. Lett. 1 (1982) 13–16.
[36] R. Morrell, Adv. Appl. Ceram. 105 (2006) 1–11.
[37] D.Q. George, C.B. Richard, J. Am. Ceram. Soc. 90 (2007) 673–680.
[38] X.M. Li, X.W. Yin, L.T. Zhang, L.F. Cheng, Y.C. Qi, J. Chin. Chem. Soc. 36 (2008) 769–775.
[39] D.C.C. Lam, F.F. Lange, A.G. Evans, J. Am. Ceram. Soc. 77 (1994) 2113–2117.
[40] D.M. Liu, Ceram. Int. 23 (1997) 135–139.
[41] R.W. Rice, J. Mater. Sci. 31 (1996) 102–118.
[42] M. Kitayama, K. Hirao, M. Toriyama, S. Kanzaki, J. Ceram. Soc. Jpn. 108 (2000) 646–649.
[43] G.H. Peng, G.J. Jiang, W.L. Li, B.L. Zhang, L.D. Chen, J. Am. Ceram. Soc. 89 (2006) 3824–3826.